Steel and Composite Structures, *Vol. 25, No. 4 (2017) 457-472*
DOI: https://doi.org/10.12989/scs.2017.25.4.457

Behavior of concrete-filled round-ended steel tubes under bending

Fa-xing Ding, Tao Zhang, Liping Wang* and Lei Fu

School of Civil Engineering, Central South University, Changsha, Hunan Province, 410075, P.R. China

(*Received April 06, 2017, Revised July 11, 2017, Accepted September 01, 2017*)

Abstract. The objective of this paper is to investigate the flexural behavior of concrete-filled round-ended steel tubes (CFRTs) under bending. Beam specimens were tested to investigate the mechanical behavior of the CFRTs, including four CFTs with different concrete strengths and steel ratios, and three CFRTs with varied aspect ratios. The load vs. deflection relationships and the failure modes for CFRTs were analyzed in detail. The composite action between the core concrete and steel tube was also discussed and examined based on the experimental results. In addition, ABAQUS program was used to develop the full-scale finite element model and analyze the effect of different parameters on the moment vs. curvature curves of the CFRTs bending about the major and minor axis, respectively. Furthermore, design formulas were proposed to estimate the ultimate moment and the flexural stiffness of the CFRTs, and the simplified theoretical model of the moment vs. curvature curves was also developed. The predicted results showed satisfactory agreement with the experimental and FE results. Finally, the differences of the experimental, FE and predicted results using the existing codes were illustrated.

Keywords: concrete-filled round-ended steel tube (CFRT); flexural behavior; ultimate moment; finite element analysis; full-scale model; composite action

1. Introduction

Concrete-filled steel tubular (CFT) structures are now extensively used in civil engineering structures, which ideally combine the advantages of both steel and core concrete: namely high strength, high ductility and fast construction (Chang *et al.* 2012, 2013, Hassanein *et al.* 2012, 2013). With these advantages, the research interest in the performance of CFT structures is continuing, such as recent publications (Aslani *et al.* 2015, Kim *et al.* 2013, Wan *et al.* 2013, Wang *et al.* 2016). In order to meet the requirement of the flexural stiffness as beam members, a new form of composite section, the concrete-filled round-ended steel tubular section (CFRT), was proposed as shown in Fig. 1 and has already been applied in bridges (Xie *et al.* 2011). The CFRT members have good architectural esthetics, and can effectively reduce the impact of fluid load on the pier attributing to the round shape at the corners.

So far, a number of experimental and numerical studies have been carried out on the behavior of CFTs under bending, such as Chen *et al.* (2015), Chen *et al.* (2016), Chitawadagi *et al.* (2009), Han *et al.* (2006), Moon *et al.* (2012), Uenaka *et al.* (2008, 2016), Wang *et al.* (2014) etc. Chen *et al.* (2016) reported the behavior of thin-walled dodecagonal section double skin concrete-filled steel tubes under bending and the design method was proposed. Chitawadagi *et al.* (2009) carried out experimental study on the flexural performance of CFT members with circular sections. Moon *et al.* (2012) conducted finite element analysis (FEA) to study the flexural performance of CFT members with circular sections. Uenaka *et al.* (2008, 2016) studied the flexural behavior of concrete filled double skin circular tubular (CFDST) under pure bending. Wang *et al.* (2014) presented the experimental investigation on the mechanical behavior of square and rectangular section CFTs, and discussed the composite action between the core concrete and steel tube.

Recently, Ding *et al.* (2015, 2016) conducted a series of tests on the CFRT columns and track-shaped rebar stiffened concrete-filled round-ended steel tube (SCFRT) columns, and investigated the effects of several important parameters, including the concrete strength, steel strength, wall thickness of the steel tube and the aspect ratio, on the structural behavior of the columns. FE models were established to analyze the composite action between the steel tube, core concrete and rebars. Finally, a practical calculation formula was proposed to estimate the ultimate bearing capacity. However, up to now there is no research reported on the CFRT under bending, and the flexural behavior of CFRT members is unknown, which may prevent them from being applied in the engineering practice.

Therefore, a further study on the flexural behavior of CFRT members based on the existing research (Ding *et al.* 2015, 2016, Liu *et al.* 2016) was carried out. The main contents of this paper include: (1) Flexural tests were conducted on seven specimens. The influence of some critical parameters on the behavior of specimens was discussed in detail. (2) Finite element models were created and validated by experimental results with reasonable constitutive models. Based on the validated FE modeling approach, an extensive parametric study was performed on

*Corresponding author, Lecturer,
E-mail: wlp2016@csu.edu.cn; kachywlp@gmail.com

http://www.techno-press.org/?journal=scs&subpage=6

ISSN: 1229-9367 (Print), 1598-6233 (Online)

Table 1 Properties of specimens and comparison between experimental and FE results

Specimens	$B\times D\times t$ (mm)	D/t	B/D	L (mm)	f_{cu} (MPa)	f_s (MPa)	M_u (kN.m) Ex	M_u (kN.m) FE	EI (kN.m^2) Ex	EI (kN.m^2) FE
CR-t3-50-1	165×165×2.70	61.1	1	1500	46.3	350	28.26	28.42	1.40	1.43
CR-t3-60-1	165×165×2.74	60.2	1		57		28.61	31.32	1.52	1.57
CR-t3-80-1	165×165×2.75	60	1		77.2		30.07	31.23	1.67	1.71
CR-t4-80-1	165×165×3.93	42	1		77.2		40.58	43.31	1.93	2.09
CR-t3-40-1	200×200×2.77	72.2	1	3000	37.7	345	51.42	50.41	2.92	3.07
CR-t3-40-1.5	300×200×2.77		1.5				100.81	98.02	7.45	7.75
CR-t3-40-2	400×200×2.77		2				180.02	184.73	18.75	19.51

the mechanical performance of the CFRTs using the full scale models. (3) According to the FE results, the practical formulas of the flexural stiffness and ultimate moment were established, and the simplified model of moment vs. curvature curves for the CFRTs was also proposed. (4) The difference between the proposed formula and current design methods for the flexural stiffness and ultimate moment of CFRTs with large dimensions were evaluated. In addition, the rationality of the proposed practical formulas was verified.

2. Experimental investigation

2.1 Test specimens and materials

Seven specimens were designed for the bending tests, and the parameters considered in the bending tests included concrete strength, wall thickness of the steel tube and aspect ratio. The cross-sectional dimensions of the CFRT specimens are shown in Fig. 1, where B (longer side) is the out-to-out dimension in the minor axis direction of the cross-section; D (shorter side) is the out-to-out dimension in the major axis direction of the cross-section and also the diameter of the two semi-circles of the cross-section; t is the wall thickness of the steel tube and L is the longitudinal dimension of the specimen. D/t is the diameter-thickness ratio of the tubular sections. The detailed information of the specimens is also summarized in Table 1.

The cross-section shape of CFRTs is variable with the change of aspect ratio (B/D), which is defined herein as B divided by D. The cross-section of CFRTs with B/D =1 is a circular CFT, namely concrete-filled circular tube (CFT), being a special case of CFRTs. The aim of the paper is to investigate CFRTs including both the special case (CFTs) and normal cases. Given the limitations on the number of tests performed, the influence of concrete strength and diameter-thickness ratio on the moment capacities of CFRTs will be obtained based on the test results of CFTs (CFRTs with B/D=1). The influence of these parameters for CFRTs with other aspect ratios will be evaluated through a parametric study.

In this study the test specimens were labeled such that the type of the specimens, the nominal thickness of the steel tube, the concrete strength, and the aspect ratio can be identified from the label. For example, the label "CR-t3-60-1" defined the specimens as follow: the first group of letter indicates the section type of the specimens, where the prefix letter "CR" refers to concrete-filled round-ended steel tube. The following digits "t3" are the nominal thickness of the steel tube. The following digits "60" indicate the concrete strength. The last digit "1" refers to the aspect ratio (B/D).

The CFRT specimens were fabricated in two steps. Firstly, flat steel plates were molded into U-shaped sections. Then two U-shaped sections were welded together with single bevel butt welds. The inside surfaces of the steel tubes were brushed to remove any possible rust and loose debris. Before pouring concrete, the cover plate was initially welded to one end of the steel tube and then the steel tube was placed upright. Concrete was poured from the top of the specimens and carefully vibrated using a vibrator to make the concrete evenly distributed inside the tube. Meanwhile, the standard concrete cubes with a dimension of 150 mm were prepared and cured under the same condition as the concrete adopted in specimens. After one month, the concrete surface of the test specimen was polished with grinder and both surfaces of concrete and steel tube were at the same level.

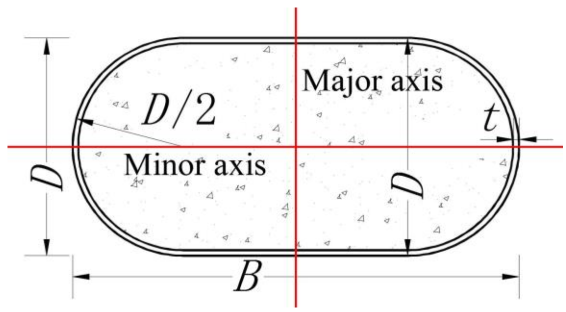

Fig. 1 Cross-section of the CFRTs

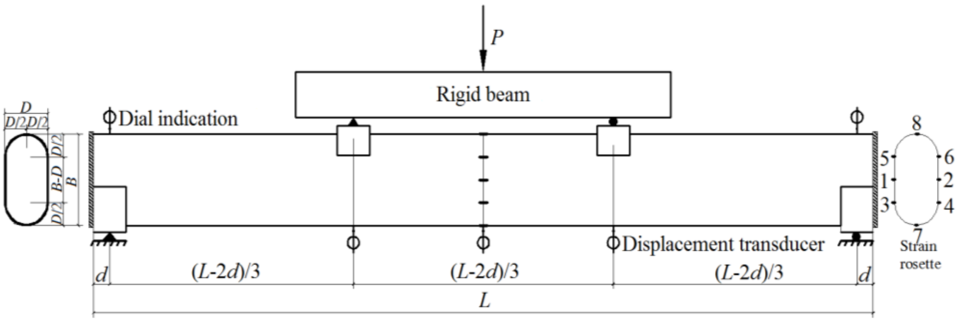

(a) Schematic view

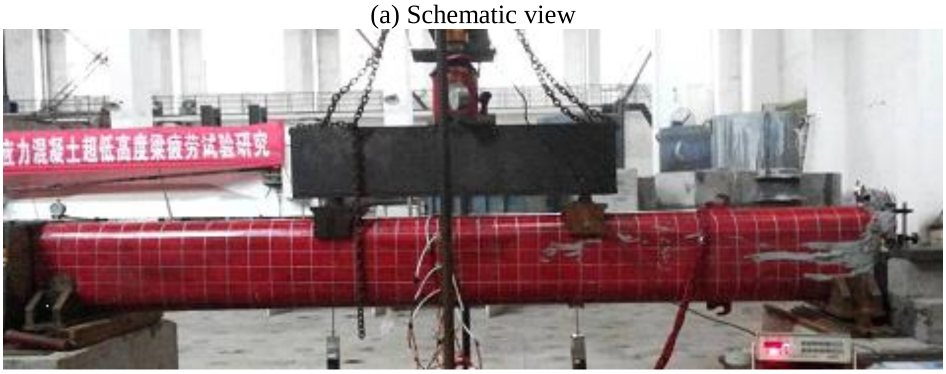

(b) Experimental setup

Fig. 2 Experimental instrumentation for all specimens

Before the bending tests of the specimens, material testing was carried out to obtain the respective material properties. The cubic compressive strength of concrete was obtained from the concrete cubes in accordance with the standard GB 50081-2002. Tensile coupon tests were carried out to obtain the material properties of the steel according to the standard GB 228-2002. The detailed material properties are listed in Table 1.

2.2 Experimental setup and instrumentation

All the tests were conducted under four-point bending with simply supported condition in the National Engineering Laboratory for high-speed railway construction technology of Central South University. The load was applied to the specimens using the 50 t hydraulic jack. To accurately measure the deformation, eight strain rosettes were attached around the surface of the specimen at the mid-span and three LVDTs were placed under the mid-span and two loading points of the specimen, respectively. In addition, two dial indications were fixed at the two ends of the specimen to measure the displacement of the test frame during the test, as shown in Fig. 2(a).

The test was carried out using load control in the elastic stage, with a force increment of 1/20 of the predicted ultimate load. After the load reached 70% of the predicted ultimate bearing capacity, the test was switched to displacement control with an increment of 0.2 mm until the predicted ultimate load was reached. The specimens were loaded at a step of 0.5 mm and maintained 5 min for each step in the post-ultimate stage. A data acquisition system was used to record the applied load and the reading of the transducers and strain rosettes at regular intervals during the tests. When the mid-span deflection of the specimen reached about 3% of the length of the specimen, the test was stopped. Fig. 2(b) gives an overall view of the experimental setup.

3. Experimental results and discussion

3.1 Load vs. deflection curves and failure modes

Based on the test observation and the measured load (P) vs. mid-span deflection (y) curves of specimens, as shown Fig. 3, the specimens generally are considered to experience three stages under bending until failure.

In the early stage of loading, there was generally a linear relation response between load and mid-span deflection, in which the load increased sharply, whereas the increase of the deflection was very limited.

For all the specimens, the steel tube started to yield and the load vs. mid-span deflection curves began to demonstrate an elastic-plastic behavior when the imposed load reached about 70% of the ultimate load.

The applied load of the specimens increased slowly while the deflection increased sharply when the ultimate load was approaching. It can be seen from Fig. 3 that there is no obvious descending in the curves, which indicates the good ductility of the specimens under bending.

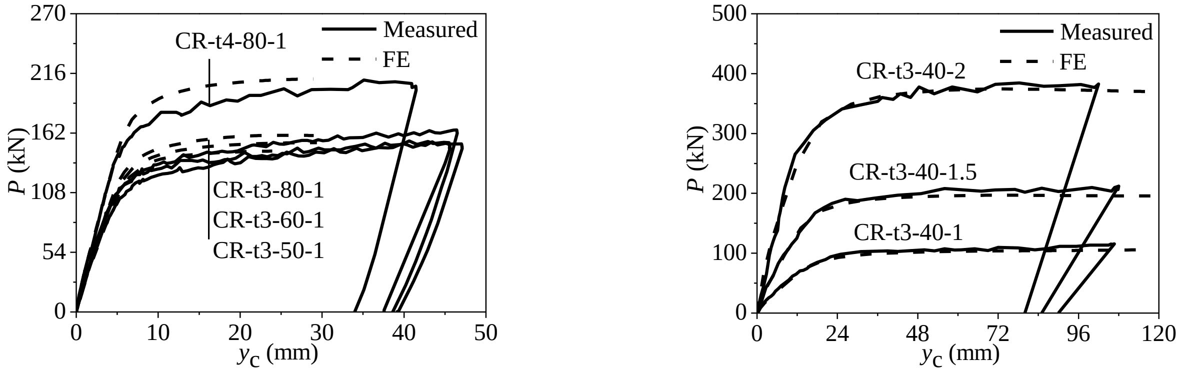

(a) (b)

Fig. 3 Comparison of load vs. mid-span deflection curves

(a) (b)

Fig. 4 Typical failure modes of the specimens

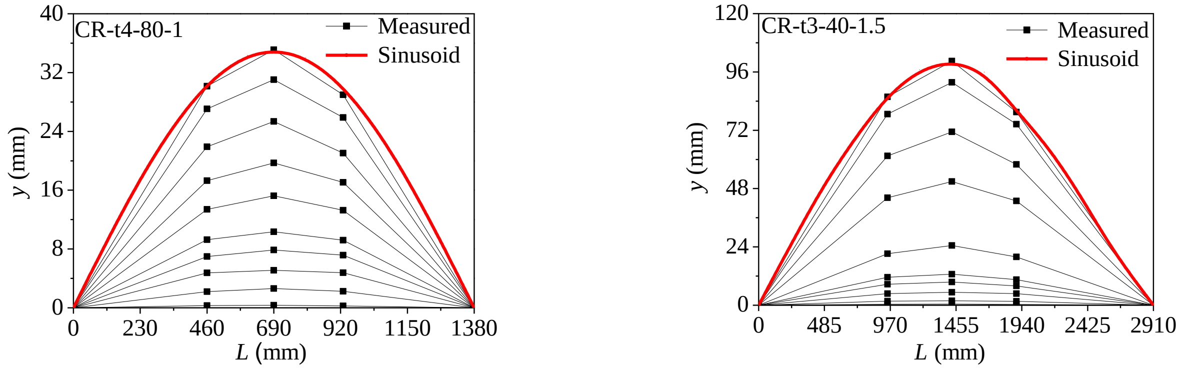

(a) CR-t4-80-1 (b) CR-t3-40-1.5

Fig. 5 Typical deflection curves of the specimen

Fig. 4 shows the typical failure modes of the specimens. All of the test specimens failed in a very ductile manner. It is found that the aspect ratio (B/D) has no significant effect on the failure mode, and the failure mode of all the specimens is the same. In addition, no tensile fracture and welding failure was observed, and there is no outward local bucking occurred on the compressive zone of the steel tube. Two typical sets of deflection curves for the CR-t4-80-1 and the CR-t3-40-1.5 specimen are shown in Fig. 5. It is shown in Fig. 5 that the measured deflection curves are in the shape of a half-sine wave.

3.2 Load vs. strain curves

Typical load vs. strain curves of the test specimens are shown in Fig. 6. The measured strains were used to determine the curvature of the beams. It is shown that the compressive and tensile strains increased linearly and slowly at the initial stage. After the yielding of steel, the compressive and tensile strain increased quickly.

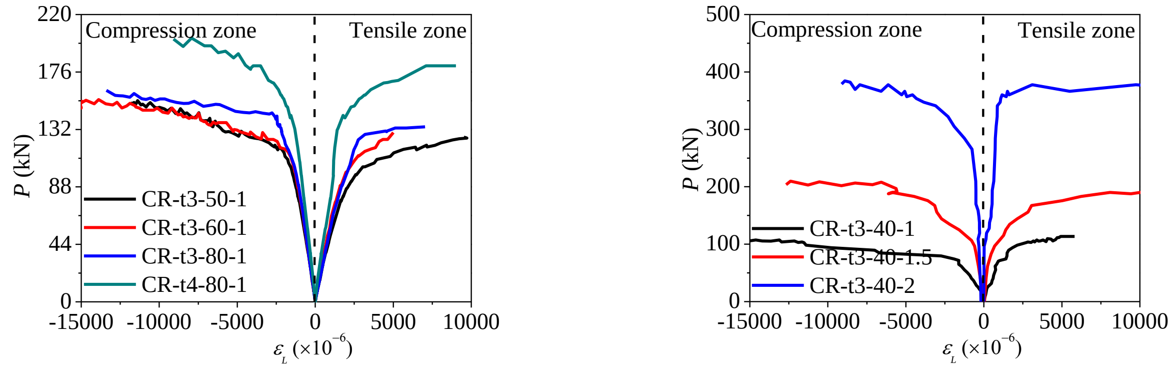

(a) (b)

Fig. 6 Load vs. strain curves of test specimens

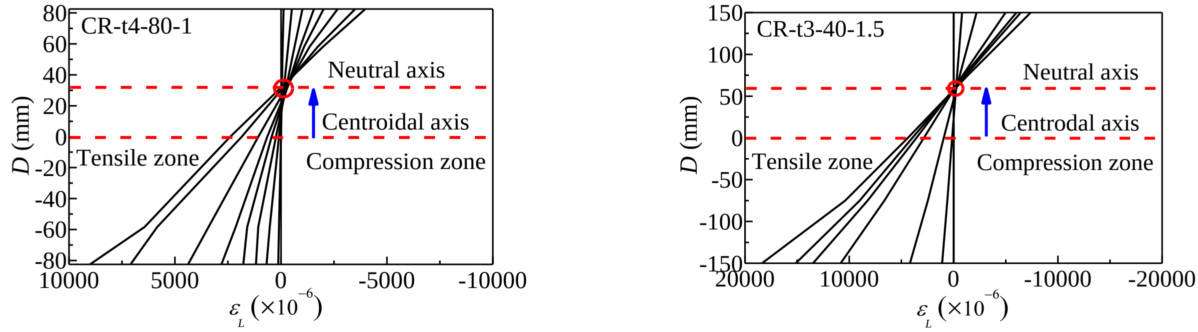

(a) CR-t4-80-1 (b) CR-t3-40-1.5

Fig. 7 Strain distribution of test specimens

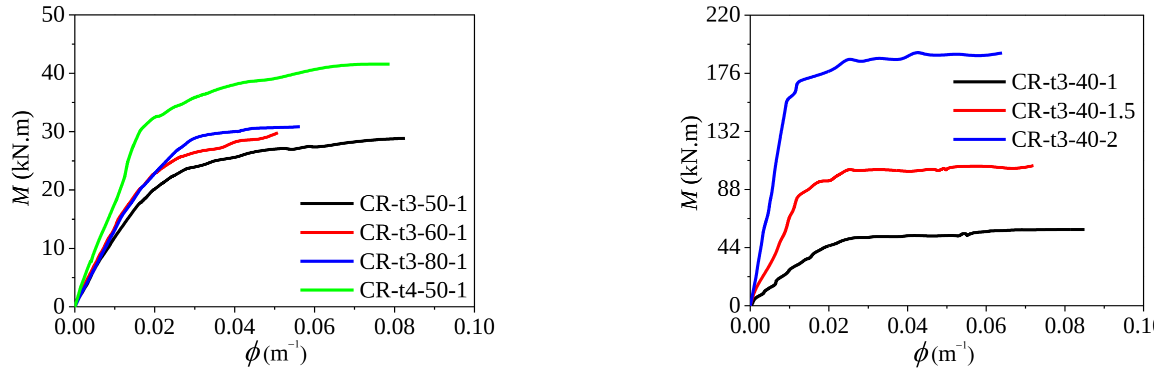

(a) (b)

Fig. 8 Comparison of typical moment vs. curvature curves of specimens

Fig. 7 shows the strain distribution along the height of the cross section of specimens, where the signs of compressive and tensile strain are defined as negative and positive respectively. It can be seen from Fig. 7 that the strain development in the compression zone is less than that in the tension zone, which could be explained by the contribution from the concrete in compression. Meanwhile, with the increase of load, the neutral axis moves upwards from the centroidal axis of section. The intersecting point of the mid-span strain curves represents the position of neutral axis of the plane. The results were consistent with the assumption of planar cross-section behavior at the mid–span of the specimens.

3.3 Bearing capacity

Fig. 8 presents the measured moment (M) vs. curvature (ϕ) curves for all the specimens.

The concrete strengths of CR-t3-60-1 and CR-t3-80-1 specimen were higher by 23.1% and 66.7% compared to

CR-t3-50-1 specimen, whereas, the ultimate moment capacities of CR-t3-60-1 and CR-t3-80-1 specimen were slightly improved by 3% and 5%, respectively. The comparison reflects that the concrete strength has slight influence on the ultimate moment capacity of the specimens.

In comparison to CR-t3-80-1 specimen, the ultimate moment capacity of CR-t4-80-1 specimen was improved by 30.7% with a 30% decrease of the diameter-thickness ratio (*D/t*). Therefore, it is indicated that the diameter-thickness ratio has moderate influence on the ultimate moment capacity of the specimens.

The aspect ratios (CR-t3-40-1, CR-t3-40-1.5 and CR-t3-40-2) were 1, 1.5 and 2, and the corresponding ultimate moment capacities were improved by 88% and 256% compared to CR-t3-40-1 specimen. The results reveal that the aspect ratio has a significant effect on the ultimate moment capacity of the specimens.

3.4 Flexural stiffness

The comparison of the flexural stiffness for all specimens was obtained from the measured moment (*M*) vs. curvature (ϕ) curves in the tests and is shown in Fig. 9.

Compared to CR-t3-50-1 specimen, the concrete strengths of CR-t3-60-1 and CR-t3-80-1 specimens were increased by 23.1% and 66.7%, and the corresponding Young's modulus were increased by 7.2% and 18.5% respectively. However, the flexural stiffness was only improved by 8.9% and 19%, respectively. It is demonstrated that the concrete strength has no obvious influence on the flexural stiffness of the specimens.

The comparison between CR-t3-80-1 and CR-t4-80-1 specimen showed that the flexural stiffness was improved by 15% with a 30% decrease of the diameter-thickness ratio (*D/t*). Therefore, it can be concluded that the diameter-thickness ratio has slight influence on the flexural stiffness of the specimens.

The aspect ratios (CR-t3-40-1, CR-t3-40-1.5 and CR-t3-40-2) were 1, 1.5 and 2, and the corresponding flexural stiffness was improved by 155% and 541% compared to CR-t3-40-1 specimen. The results indicated that the aspect ratio has the most significant effect on the flexural stiffness of the specimens.

3.5 Strain ratio

The strain ratio (v_{sc}) is defined herein as the absolute value of the circumferential strain divided by the axial strain of the steel tube. Larger strain ratio indicates higher confinement level of the core concrete provided by the steel tube. Fig. 10 shows the relationships of the measured load (*P*) versus the strain ratio (v_{sc}) of all specimens, where the sign of strain ratio is defined as negative in the compression zone and positive in the tensile zone of the cross-section under bending.

It can be seen from Fig. 10 that the measured strain ratio is nearly constant and approximately equivalent to Poisson's ratio of steel at the initial stage. It is indicated that there is negligible confinement effect between the steel tube and core concrete. The strain ratio in the compressive zone began to increase sharply when the imposed load is around 70% of the ultimate bearing capacity. This indicated that the steel tube started to produce a significant confinement effect on the core concrete. On the contrary, the strain ratio in the tensile zone decreased slowly with the increase of applied load, which reflected that the confinement effect was smaller in the tensile zone than in the compression zone.

4. Finite element (FE) modeling

4.1 FE models

Finite element (FE) models were developed using the finite element package ABAQUS (Hibbitt *et al.* 2003).

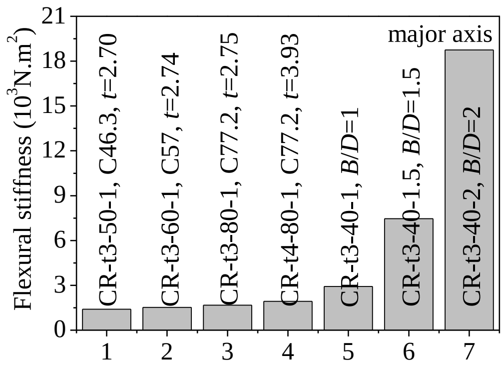

Fig. 9 Comparison of the flexural stiffness for all specimens bending about the major axis

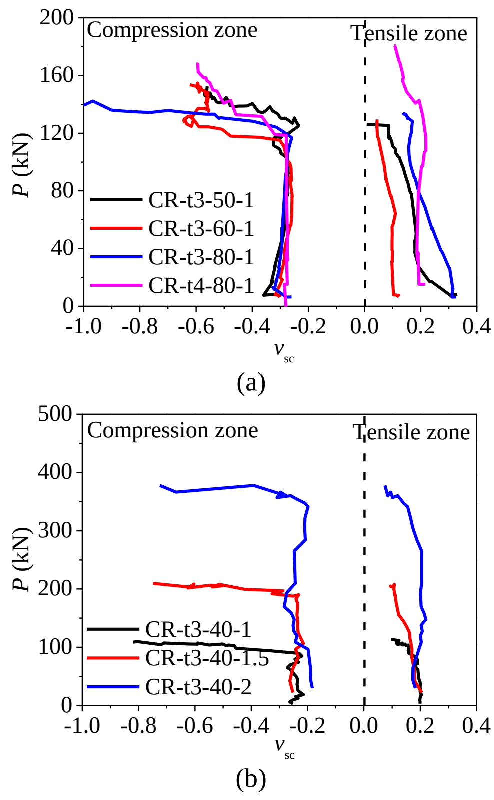

Fig. 10 Comparison of load vs. strain ratio curves from the experimental results

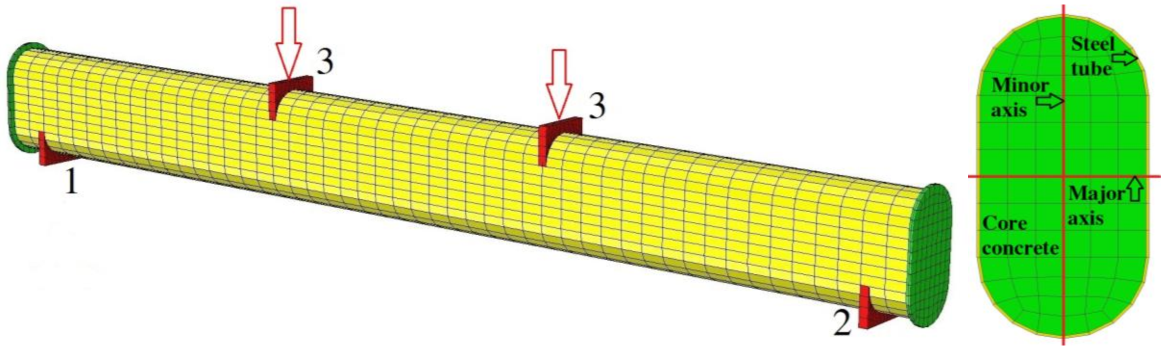

Fig. 11 FE model after meshing

In these models, the 8-node reduced integral format 3D solid element (C3D8R) was chosen to model the core concrete, steel tube and cover plate for all specimens. A surface-based interaction with "hard" contact in the normal direction and the Coulomb friction coefficient of 0.5 in the tangential direction of the interface was used to simulate the interfacial behavior between the steel tube and core concrete, in which the sliding formulation is finite sliding. A tie constraint may couple two separate surfaces so that no relative motion would occur. Therefore, the tie option was adopted for the constraint between the cover plate and the concrete as well as the steel tube at two ends of the specimens.

The model was loaded under four-point bending, which was consistent with the tests. In the FE model, both the support and loading plates were modeled as rigid bodies. The simply supported boundary condition was modeled by releasing the in-plane rotation at the reference point 1, and releasing both the in-plane rotation and axial displacement along the specimen at the reference point 2. Considering the nonlinear calculation is more easily convergent under displacement loading, the load was applied to the specimen through the loading plates (reference point 3) by means of a specified displacement. The boundary conditions and meshing results of the FE model with the structured meshing technique are shown in Fig. 11.

4.2 Material models

The concrete damaged plasticity model and Willam-Warnke five-parameter failure criteria in Abaqus (Hibbitt *et al.* 2003) were adopted in the FE modeling for the concrete. The relevant parameters used for the material model in this study were defined according to reference (Liu *et al*. 2016). These parameters have been validated by experimental results (Ding *et al*. 2015, 2016, Liu *et al*. 2016), in which the adopted stress-strain relationships of concrete in compression and tension are applicable for concrete with strength ranging from 20 to 140 MPa. More information of the concrete model can be referred in Liu *et al*. (2016).

An elasto-plastic model, considering Von Mises yield criteria, Prandtl-Reuss flow rule, and isotropic strain hardening, was used to describe the constitutive behavior of steel. The model has been validated in prior studies (Ding *et al*. 2015, 2016, Liu *et al*. 2016), and described as follows

$$\sigma_i = \begin{cases} E_s \varepsilon_i & \varepsilon_i \le \varepsilon_y \\ f_s & \varepsilon_y < \varepsilon_i < \varepsilon_{st} \\ f_s + \zeta E_s(\varepsilon_i - \varepsilon_{st}) & \varepsilon_{st} < \varepsilon_i \le \varepsilon_u \\ f_u & \varepsilon_i > \varepsilon_u \end{cases} \tag{1}$$

where, σ_i and ε_i are the equivalent stress and strain of steel. f_s, and f_u (=1.5f_s) are the yield strength and ultimate strength respectively. E_s (=2.06×10^{5}MPa) and E_{st} ($E_{st}=\zeta E_s$) are the elastic modulus and strengthening modulus. ε_y, ε_{st} and ε_u are the yield strain, hardening strain, and ultimate strain of steel, which is expressed by $\varepsilon_u = \varepsilon_{st} + 0.5f_s/(\zeta E_s)$, where $\varepsilon_{st}=12\varepsilon_b$, $\varepsilon_u=120\varepsilon_b$ and $\zeta=1/216$.

4.3 Experimental verification

The comparison of experimental and corresponding FE results is shown in Table 1. Good correspondence is found in general and the discrepancies between experimental and corresponding FE results are less than 8% for all the specimens. In addition, the load vs. mid-span deflection curves and the moment vs. curvature curves of experimental and corresponding FE results are shown in Figs. 3 and 12, respectively. The results from Figs. 3 and 12 show that the predicted curves agree reasonably well with the experimental results. Besides, existing experimental data (Han *et al*. 2006) was also collected to further verify the accuracy of the established FE model, as shown in Fig. 13. It is shown that the FE modeling curves agree well with the experimental results, especially for the elastic stage and ultimate bearing capacity. Therefore, the FE model and the material constitutive model adopted in this study were proved to be reasonable and adequate.

4.4 Parametric study

The cross-section dimensions of the test specimens were usually smaller than that in practice due to the equipment limitation. Therefore, full-scale models based on the validated FE modeling approach were developed to extensively investigate the influence of parameters on the mechanical performance of the CFRTs under bending. Numerical analysis on a total of 696 FE specimens were performed to investigate the following parameters: bending direction, steel strength ranging from 235 MPa to 420 MPa, concrete strength covering from C40 to C100 (the scope of material in steel and concrete is commonly used in engineering practice), steel ratio from 0.02 to 0.08 and the aspect ratio ranging from 1 to 4. The following steel and concrete were paired for the specimens: Q235 (the digits in the steel grades indicate the nominal yield strength of steel, similarly hereinafter) steel were paired with C40 and C60 concrete, Q345 steel were paired with C60 and C80 concrete, and Q420 steel were paired with C80 and C100 concrete. The detailed parameters used in the calculation are summarized in Table 2. The following will take the specimens with D=1200 (B/D=1, 2, 3 and 4) as examples.

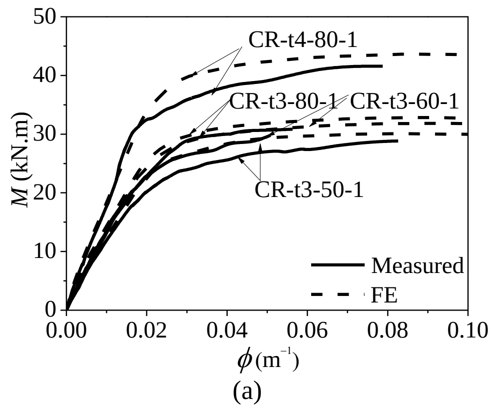

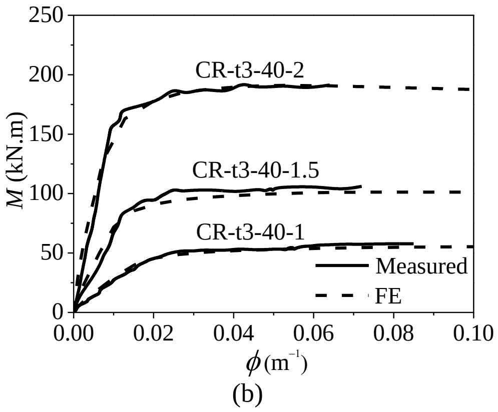

Fig. 12 Comparison of moment vs. curvature curves of specimens between FE and experimental results

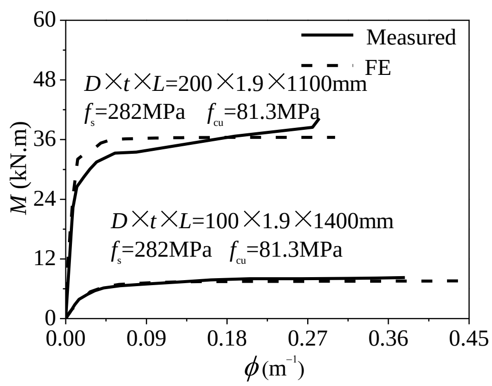

Fig. 13 Comparison of moment vs. curvature curves of specimens from Han *et al*. (2006)

Table 2 Geometric sizes of specimens for FE parametric study

D (mm)	B (mm)	t (mm) ρ_s=0.02	ρ_s=0.05	ρ_s=0.08	L (mm)
300	300	1.48	3.62	5.66	2700
	600	2.05	5.01	7.84	5400
	900	2.30	5.62	8.78	8100
	1200	2.44	5.96	9.30	10800
600	600	2.96	7.23	11.32	5400
	1200	4.10	10.02	15.68	10800
	1800	4.60	11.24	17.56	16200
	2400	4.89	11.91	18.60	21600
900	900	4.43	10.85	16.99	8100
	1800	6.15	15.04	23.53	16200
	2700	6.91	16.85	26.34	24300
	3600	7.33	17.87	27.90	32400
1200	1200	5.91	14.46	22.65	10800
	2400	8.21	20.05	31.37	21600
	3600	9.21	22.47	35.12	32400
	4800	9.77	23.82	37.20	43200
1500	1500	7.39	18.07	28.31	13500
	3000	10.26	25.06	39.21	27000
	4500	11.51	28.09	-	40500
	6000	12.21	29.78	-	54000

4.4.1 Steel strength

Fig. 14(a) presents the effect of steel strength on the moment vs. curvature curves of the specimens. No significant difference was observed in the elastic stage. Comparison of the flexural stiffness among specimens with varied steel strengths is shown in Fig. 15(a). The steel strengths are 235 MPa, 345 MPa and 420 MPa, respectively, while other parameters were kept the same for two specimens bending about the major axis in comparison. It can be found from Figs. 14(a) and 15(a) that with increase of steel strength, the ultimate moments were improved by 36% (from 235 MPa to 345 MPa) and 17% (from 345 MPa to 420 MPa), while the flexural stiffness almost remained the same for specimens bending about the major axis. Therefore, the steel strength can help to increase the ultimate moment. Similar conclusion can be drawn from Figs. 14(a) and 15(a) for the specimens bending about the minor axis.

4.4.2 Concrete strength

Fig. 14(b) illustrates the effect of concrete strength on the moment vs. curvature curves of the specimens. The comparison of the flexural stiffness among specimens with varied concrete strengths is given in Fig. 15(b). The concrete strengths are C40, C60, C80 and C100, respectively. It was observed from Figs. 14(b) and 15(b) that there was no obvious difference in the elastic stage. With the increase of concrete strength, the corresponding Young's modulus was increased about 14.5% (from C40 to C60), 10% (from C60 to C80) and 7.7% (from C80 to C100), the ultimate moment was slightly improved by less than 5%, and the flexural stiffness almost remained unchanged. It can be concluded that the concrete strength has slight effect on the mechanical performance.

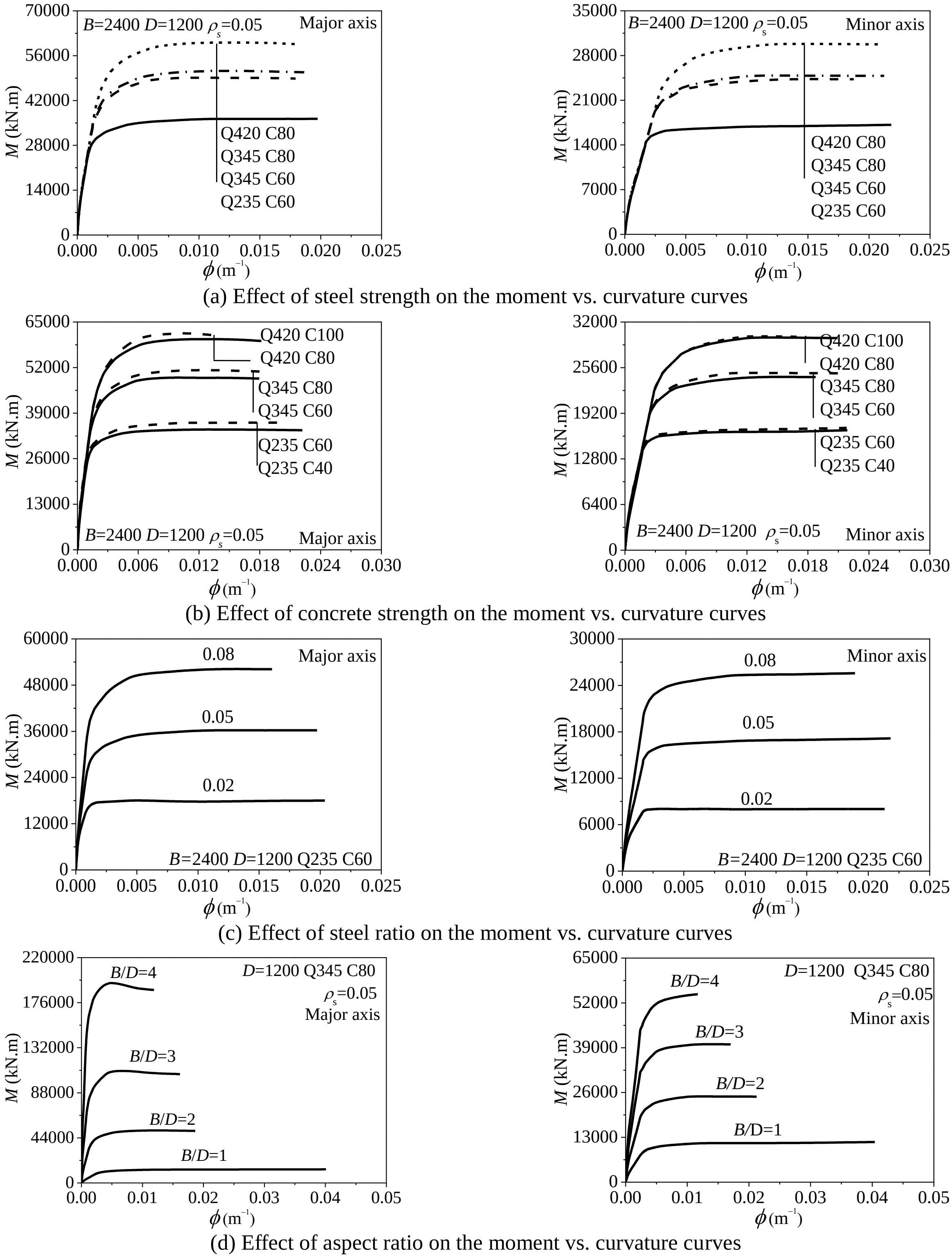

(a) Effect of steel strength on the moment vs. curvature curves

(b) Effect of concrete strength on the moment vs. curvature curves

(c) Effect of steel ratio on the moment vs. curvature curves

(d) Effect of aspect ratio on the moment vs. curvature curves

Fig. 14 Comparison of moment vs. curvature curves of specimens with different parameters

4.4.3 Steel ratio

The steel ratio is an important parameter for the structural performance of CFTs according to extensive previous research. The steel ratio (ρ_s) is defined as the steel area (A_s) divided by the total cross-sectional area (A_{sc}), as follows: $\rho_s=A_s/A_{sc}$.

Fig. 14(c) illustrates the effect of the steel ratio on the moment vs. curvature curves of the specimens. The comparison of the flexural stiffness among the specimens with varied steel ratios is shown in Fig. 15(c). The steel ratios are 0.02, 0.05 and 0.08, respectively. It can be found from Figs. 14(c) and 15(c) that with the increase of steel

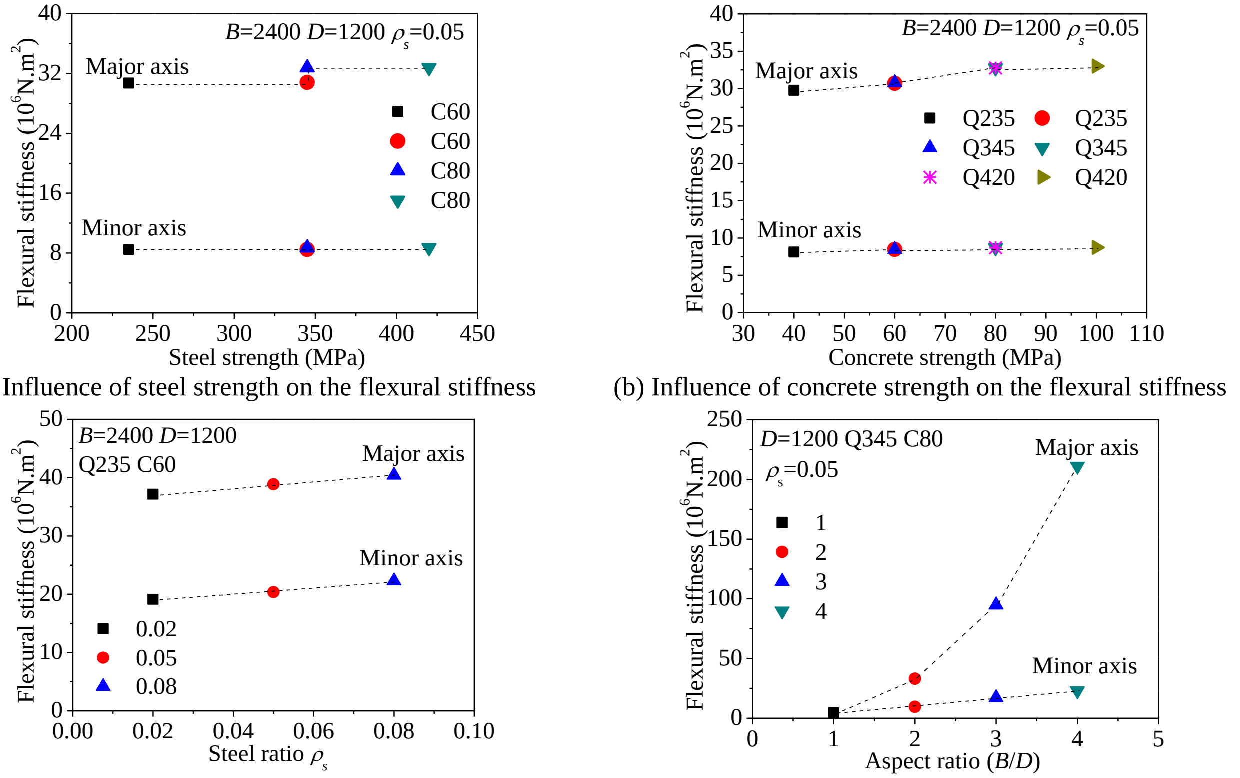

(a) Influence of steel strength on the flexural stiffness

(b) Influence of concrete strength on the flexural stiffness

(c) Influence of steel ratio on the flexural stiffness

(d) Influence of aspect ratio on the flexural stiffness

Fig. 15 Influence of various parameters on the flexural stiffness

ratio from 0.02 to 0.05 and 0.05 to 0.08, the flexural stiffness of specimens bending about major axis was slightly improved by 1.2% and 6.5%, and the ultimate moment of specimens bending about major axis was improved by 103.6% and 192.7% respectively. Therefore, the steel ratio contributes to increasing the ultimate moment, whereas has almost little influence on the flexural stiffness. Similar conclusion can be drawn from Figs. 14(c) and 15(c) for the specimens bending about the minor axis.

4.4.4 Aspect ratio

Fig. 14(d) shows the effect of the aspect ratio (*B/D*) on the moment vs. curvature curves of the specimens. The comparison of the flexural stiffness among the specimens with varied aspect ratios (*B/D*) is shown in Fig. 15(d). The aspect ratios (*B/D*) are 1, 2, 3 and 4 respectively. It was found that the flexural stiffnesses of specimens bending about major axis were improved by 7.5, 21.5 and 47.9 times, and corresponding ultimate moments were improved by 3.8, 8.2 and 14.8 times respectively, as the aspect ratio increased from 1 to 2, 3, and 4. Moreover, the flexural stiffnesses of specimens bending about minor axis were improved by 2.1, 3.9 and 5.2 times, and corresponding ultimate moments were improved by 1.9, 3.0 and 4.1 times respectively, as the aspect ratio increased from 1 to 2, 3, and 4. The results show that the aspect ratio (*B/D*) has much more significant influence on the flexural performance of the specimens bending about the major axis than those bending about the minor axis.

5. Design approach

Different design methods were used to predict the ultimate strength of the CFTs. It should be noted that the current design methods are applicable for the CFTs with circular sections and the CFRTs were not covered. Therefore, a new method for the CFRTs was proposed based on the experimental and FE results in this study.

5.1 Flexural stiffness

The flexural stiffness of composite members is calculated by

$$(EI)_{sc} = E_s I_s + k_z E_c I_c \tag{2}$$

Table 3 Comparison of k_z from the different codes

Code	k_z	Section type
AISC (1999)	0.8	Circular Square Rectangle
EC4 (2004)	0.6	
AIJ (1997)	0.2	
BS5400 (2005)	0.45	
CECS28 (2012)	0.6	Circular
DBJ13-51 (2003)	0.8	

Table 4 Comparison of the flexural stiffness from experimental, FE and predicted results

Specimens	$B\times D\times t$ (mm)	EI Ex	EI FE	$EI_{Eq.(3)}$ Eq.(3)	$EI/EI_{Eq.(3)}$ Ex	$EI/EI_{Eq.(3)}$ FE
C-t3-50-1	165×165×2.70	1.40	1.43	1.59	0.88	0.91
C-t3-60-1	165×165×2.74	1.52	1.57	1.64	0.93	0.96
C-t3-80-1	165×165×2.75	1.67	1.71	1.72	0.97	0.99
C-t4-80-1	165×165×3.93	1.93	2.09	2.05	0.94	1.02
CR-t3-40-1	200×200×2.77	2.92	3.07	3.06	0.96	1.00
CR-t3-40-1.5	300×200×2.77	7.45	7.75	9.14	0.82	0.85
CR-t3-40-2	400×200×2.77	18.75	19.51	19.67	0.95	0.99
				Average	0.92	0.96
				COV	0.059	0.064

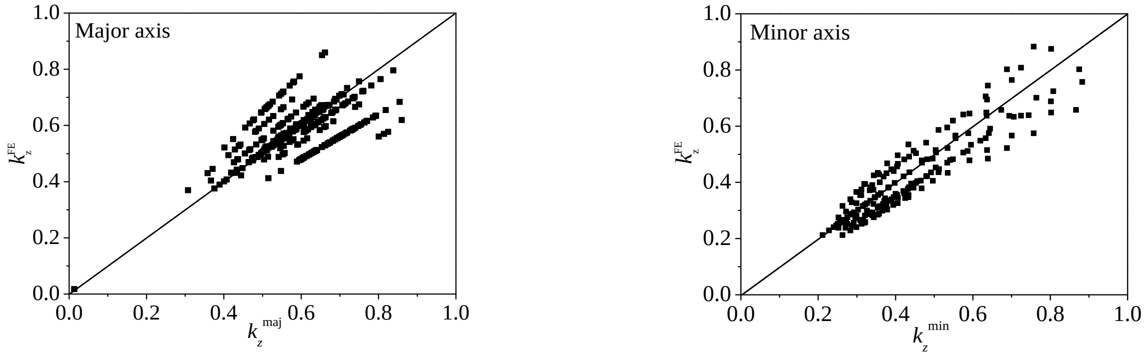

(a) Specimens bending about major axis (b) Specimens bending about minor axis

Fig. 16 Comparison of k_z between FE results and predicted results

where, E_s and E_c are the elastic modulus of steel and concrete, I_s and I_c are the moments of inertia for the steel tube and core concrete, respectively. k_z is the reduction factor for the gross stiffness of concrete. The values of k_z in different codes are summarized in Table 3.

The flexural stiffness of the specimens can be obtained from the moment vs. curvature curves, which is defined as the secant stiffness corresponding to the point with moment of $0.4M_u$. Based on the FE results and regression analysis, k_z is expressed as:

About major axis

$$k_z^{\mathrm{maj}} = 0.6\left(\frac{B}{D}\right)^{-0.61} \tag{3a}$$

About minor axis

$$k_z^{\mathrm{min}} = 0.6\left(\frac{B}{D}\right)^{-0.54} \tag{3b}$$

The comparison between the experimental, FE and predicted results is shown in Table 4. The average ratios of $EI_{Ex}/EI_{Eq\ (3)}$ and $EI_{FE}/EI_{Eq\ (3)}$ are 0.92 and 0.96 with a coefficient of variation of 0.059 and 0.064, respectively. It is shown that the predicted results by the proposed formula (Eq. (3)) are in good agreement with the experimental results.

The comparison between the FE and predicted values of k_z by Eq. (3) is shown in Fig. 16. The average ratios of the k_z^{FE}/k_z^{maj} and k_z^{FE}/k_z^{min} are 0.95 and 1.02 with a coefficient of variation of 0.090 and 0.111, respectively.

5.2 Flexural strength index

Based on the parametric studies, the ultimate moment and corresponding ultimate curvature of the CFRTs are mainly influenced by the aspect ratio. The curvature corresponding to the ultimate moment is used to describe the ductility of the CFRTs as follows:

About major axis

$$\phi_u^{maj} = 13 f_s / (E_s B) \tag{4a}$$

About minor axis

$$\phi_u^{min} = 13 f_s / (E_s D) \tag{4b}$$

The flexural strength index (γ^m) in this paper is defined based on the current standards (DBJ13-51-2003 and DL/T5085-1999) and expressed as

$$\gamma^{\mathrm{m}} = \frac{M_{\mathrm{u}}}{W_{\mathrm{sc}} f_{\mathrm{sc,u}}} \tag{5}$$

where M_u is the ultimate moment of the composite beams; W_{sc} is the section modulus of the composite beams, which is determined by

About major axis:

$$I_{maj} = \frac{D(B-D)^3}{12} + 2\left(\frac{\pi D^4}{128} - \left(\frac{2D}{3\pi}\right)^2 \frac{\pi D^2}{8} + \left(\frac{B-D}{2} + \frac{2D}{3\pi}\right)^2 \frac{\pi D^2}{8}\right),$$

$$W_{sc}^{maj} = \frac{I_{maj}}{B/2};$$

About minor axis: $I_{min}=\dfrac{D(B-D)^3}{12}+\dfrac{\pi D^4}{64}$, $W_{sc}^{maj}=\dfrac{I_{min}}{D/2}$; $f_{sc,u}$ is the "nominal yielding strength" of the composite sections calculated by $N_u = f_c A_c[1+(0.8+0.9D/B)\Phi]$ (Ding *et al*. 2015), $f_{sc,u}= N_u /A_{sc}$, in which, N_u is the axial compressive strength of the CFRT columns, Φ is the confinement factor ($\Phi=f_y A_s/f_c A_c$).

The relationship between the flexural strength index (γ^m) and the confinement factor (Φ) for the CFRTs is plotted in Fig. 17. It can be found from Fig. 17 that γ^m increases with increase of the confinement factor (Φ). The relation between γ^m and Φ of the CFRTs can be obtained by regression analysis.

About major axis

$$\gamma_{maj}^{m}=\frac{B+0.3D}{2.7B+0.35D}+(1.35-0.054B/D)\Phi \tag{6a}$$

About minor axis

$$\gamma_{min}^{m}=\frac{B}{6.31B-3.58D}+(1.36+0.16B/D)\Phi \tag{6b}$$

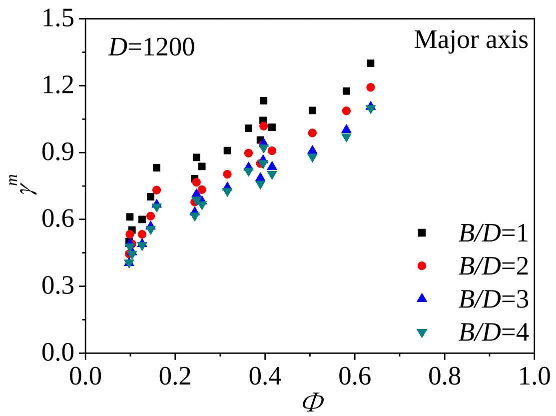

(a) Major axis D=1200

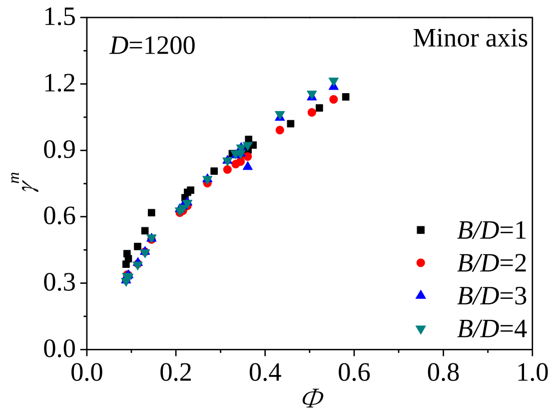

(b) Minor axis D=1200

Fig. 17 γ^m vs. Φ relation

5.3 Evaluation of the formulas

5.3.1 Ultimate moment of the CFTs

Different formulas available in the literature and standards for predicting the ultimate moment of the CFTs are summarized in Table 5.

The suitability of Eq. (5) and the formulas in Table 5 were evaluated based on the experimental results in this paper and those reported in (Han *et al*. 2006), which cover a wide range of parameters of geometry (B/D=1, $D\geq$165mm).

The predicted results ($M_{u.c}$) using different formulas were compared to the experimental results (M_u) as shown in Table 6, in which the ratios are values of experimental results divided by the corresponding predicted results.

It can be found from Table 6 that the predicted strengths by AISC, EC4 and AIJ are relative conservative, while the predicted strengths by DL/T and GB50936-2014 are slightly greater. Meanwhile, the average ratios of M_u/M_{FE}, $M_u/M_{Eq\ (5)}$ and M_u/M_{DBJ} are 0.98, 0.96 and 1.01 with the corresponding coefficients of variation of 0.055, 0.071 and 0.129, respectively. The comparisons demonstrated that the formulas proposed by Eq. (5) and DBJ are rational for predicting the moment capacities of CFTs.

The predicted strengths using different formulas were also compared with the FE results of the parametric study specimens, as shown in Table 7. The FE results covered a wide range of parameters (B/D=1, $D\geq$300 mm), and included 90 FE models bending about major axis and 90 FE models bending about minor axis. It can be seen from Table 7 that the average ratio of $M_{EF}/M_{Eq\ (5)}$ is 0.97 with a coefficient of variation of 0.043, which indicates that Eq. (5) is able to predict the ultimate moment of the CFTs with the tubular diameter up to 1500 mm.

Table 5 Formulas for the ultimate moment of the CFTs under bending

Code	Formulation
AISC-LFRD (2005)	$M_{u.c} = Zf_y$; $Z = (D^3-(D-2t))^3/6$
EC4 (2004)	$M\leq W_{ps}f_y/\gamma_s+0.5W_{pc}f_c'/\gamma_c-W_{psn}f_y/\gamma_s-0.5W_{pcn}f_c'/\gamma_c$ $W_{pc}=(D-2t)^3/4-2r^3/3$; $W_{ps}=D^3/4-2(r+t^3)/3-W_{pc}$ $W_{pcn}=(D-2t)h_n^2$; $W_{psn}=D\,h_n^2- W_{pcn}$; $r=D/2-t$ $h_n=A_c f_c/(2Df_c+4t(2f_y/\gamma_s+f_c/\gamma_c))$
AIJ(1997)	$M_{u.c} = Zf_y$; $Z = (D^3-(D-2t))^3/6$
DBJ13-51 (2003)	$M_{u.c} = \gamma_m W_{sc} f_{sc}$; $\gamma_m=1.1+0.48\ln(\xi+0.1)$
GB50936 (2014)	$M_{u.c} = \gamma_m W_{sc} f_{sc}$; $W_{sc} = \pi(r_0^4-r_{ci}^4)/4r_0$
DL/T5085 (1999)	$M_{u.c} = \gamma_m W_{sc} f_{sc}$

Table 6 Comparison between experimental, FE and predicted results using different design methods

Reference	Specimens	$D\times t\times L$ (mm)	$M_u/M_{u.c}$ FE	Eq (5)	AISC	EC	AIJ	GB	DL/T	DBJ
This paper	CR-t3-50-1	165×2.70×1500	0.99	0.89	1.26	1.07	1.26	0.93	0.98	0.90
	CR-t3-60-1	165×2.74×1500	0.91	0.90	1.26	1.00	1.26	0.88	0.85	0.89
	CR-t3-80-1	165×2.75×1500	0.94	0.92	1.32	0.91	1.32	0.84	0.71	0.90
	CR-t4-80-1	165×3.93×1500	0.94	0.89	1.26	1.03	1.26	0.88	0.86	0.89
	CR-t3-40-1	200×2.77×3000	1.01	1.07	1.52	1.31	1.52	1.14	1.23	1.10
Han *et al.* (2006)	CVB	200×1.9×1400	1.05	1.01	1.93	0.80	1.93	0.92	0.53	1.20
	CB4	180×3×900	1.07	1.01	1.71	1.07	1.71	0.91	0.72	1.14
	CB5	180×3×1800	0.99	0.96	1.62	1.02	1.62	0.87	0.68	1.08
		Average	0.98	0.96	1.49	1.14	1.49	0.92	0.82	1.01
		COV	0.055	0.071	0.170	0.122	0.170	0.102	0.258	0.129

Table 7 Comparison between FE and predicted results by various design methods

$B\times D$ (mm)	$M_{FE}/M_{u.c}$ Eq (5)	AISC	EC4	AIJ	GB	DL/T	DBJ
300×300	1.01	1.84	1.22	1.84	0.90	0.65	1.24
600×600	1.02	1.85	1.23	1.85	0.91	0.65	1.25
900×900	0.97	1.77	1.17	1.77	0.87	0.62	1.19
1200×1200	0.94	1.70	1.13	1.70	0.84	0.61	1.15
1500×1500	0.93	1.69	1.12	1.69	0.83	0.60	1.14
Average	0.97	1.77	1.17	1.77	0.87	0.62	1.19
COV	0.043	0.041	0.039	0.041	0.040	0.038	0.040

5.3.2 Ultimate moment of the CFRTs

The design method of CFRTs with B/D >1 under bending is not covered in the current design codes. Thus, the authors attempted to use the design equations in standard GB50936 and standard DL/T5058 for CFRTs with B/D =1 to calculate the ultimate moments of CFRTs with different aspect ratios (2, 3 and 4) under bending.

The comparison between the FE results and predicted strengths by the standard GB50936 and standard DL/T5058 are shown in Figs. 18 and 19, respectively. The comparison includes a total of 516 CFRTs with aspect ratios B/D = 2, 3, and 4. It can be seen from Fig. 18 that the FE results are generally smaller than the predicted results by the standard GB50936 for CFRTs with different aspect ratios (2, 3 and 4) bending about major and minor axis. The average ratios of M_{FE}/M_{GB} are 0.84 and 0.80 with the corresponding COV of 0.078 and 0.062 for beams bending about major axis and minor axis, respectively. This may be due to that the flexural strength indexes (γ^m) calculated by the standard DL/T5058 for a part of CFRT specimens are slightly greater than the actual values.

Besides, it is obvious from Fig. 19 that the FE results are far less than the predicted strengths by the standard DL/T5058 for CFRTs with different aspect ratios (2, 3 and 4) bending about both major and minor axis. The average ratios of M_{FE}/M_{DL} are 0.61 and 0.59 with the corresponding COV of 0.146 and 0.145 for beams bending about major axis and minor axis, respectively. This is because all the flexural strength indexes (γ^m) for the sections in this study are defined uniformly as 1.2 according to the standard DL/T5058, which are greater than the actual values. Therefore, this leads to the unsafety for the design equations in the standard DL/T5058.

The ultimate moments of the CFRTs obtained from experiments, FE analysis and Eq. (5) were compared as shown in Table 8. The average ratios of $M_u/M_{Eq\ (5)}$ and M_u/M_{FE} are 1.0 and 1.02 with the corresponding coefficients of variation of 0.038 and 0.020, respectively.

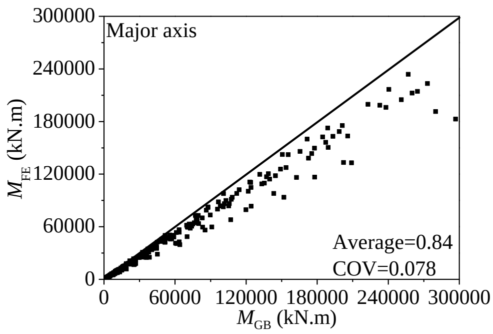

(a) Major axis

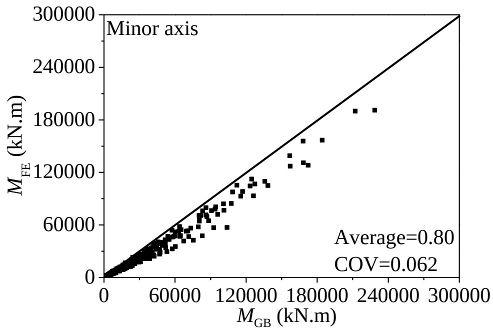

(b) Minor axis.

Fig. 18 Comparison between FE and predicted results for CFRTs by the standard GB50936

Table 8 Comparison between experimental, FE and predicted results

Specimens	M_u	$M_{u.c}$				$M_u/M_{u.c}$			
	Ex	FE	Eq.(5)	GB	DL	FE	Eq.(5)	GB	DL
CR-t3-40-1.5	100.81	98.02	97.42	134.52	136.29	1.03	1.03	0.75	0.74
CR-t3-40-2	180.02	184.73	179.03	195.62	207.20	0.97	1.01	0.92	0.87
				Average		1.00	1.02	0.83	0.80
				COV		0.038	0.020	0.145	0.114

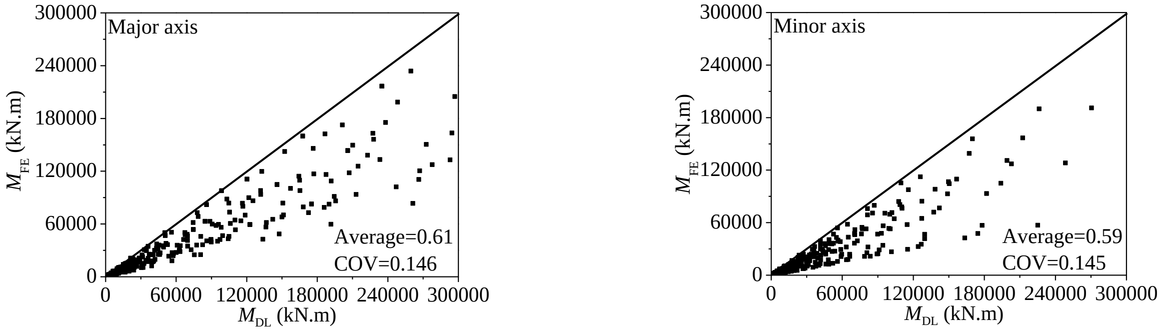

(a) Major axis (b) Minor axis

Fig. 19 Comparison between FE and predicted results for CFRTs by the standard DL/T5058

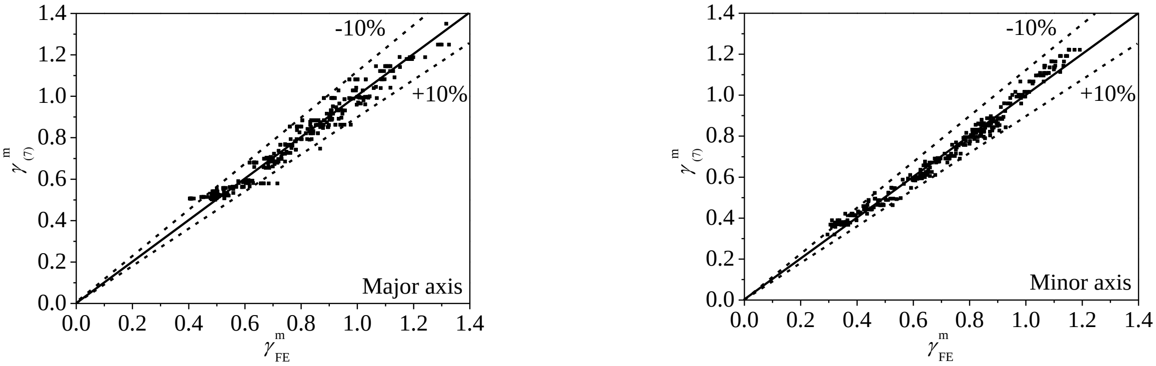

(a) Specimens bending about major axis (b) Specimens bending about minor axis

Fig. 20 Comparison of the γ^m from FE analysis and Eq. (5)

The comparison between FE and the predicted results by Eq. (5), including 258 FE models bending about major axis and 258 FE models bending about minor axis, are plotted in Fig. 20. Good agreement was achieved with the average discrepancy less than 10%. Therefore, the proposed formula (Eq. (5)) is adopted as the basic form for predicting the ultimate moment of CFRTs.

5.4 Moment versus curvature relationship

Based on the regression analysis, a simplified model for calculating the moment (M) vs. curvature (ϕ) relationship of the CFRTs was established as follows

$$y = \begin{cases} \dfrac{kx + (m-1)x^2}{1 + (k-2)x + mx^2} & x \le 1 \\ 1 & x > 1 \end{cases} \tag{7}$$

where $y = M/M_u$, $x = \phi/\phi_u$, $k = E_s I_s \times \phi_u / M_u$, $m = 1.6(k-1)^2$.

The moment vs. curvature curves obtained from experimental, FE and the Eq. (7) were compared as shown in Fig. 21 for the test specimens and Fig. 22 for the parametric specimens. It can be seen from Fig. 21 and Fig. 22 that the proposed formula (Eq. (7)) can predict well of the M vs. ϕ relationship for both the CFTs and CFRTs under bending.

6. Conclusions

This paper presents a combined experimental and numerical study on the behavior of the CFRTs under bending. Parametric study was also performed to understand the influence of different parameters on the behavior of the CFRTs. Based on the results of the current study, the following conclusions can be drawn:

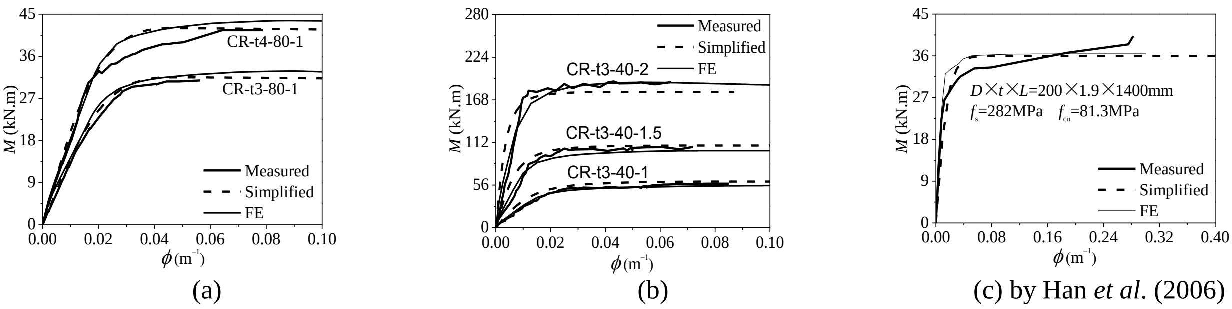

Fig. 21 Comparison of moment vs. curvature curves between experimental, FE and predicted results

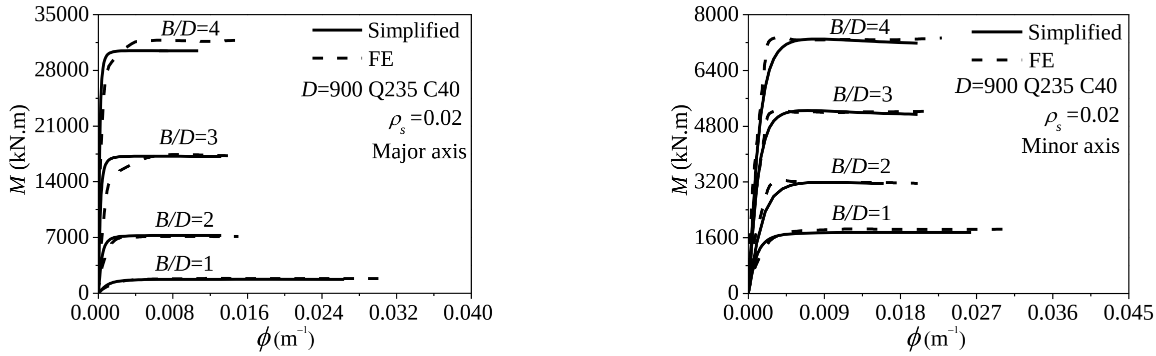

Fig. 22 Comparison of moment vs. curvature curves between FE and predicted results

(1) Seven CFRTs were tested under bending. It was observed that the specimens experienced three stages: elastic stage, elastic-plastic stage and plastic stage during the loading process. The confinement effect of the steel tube on the core concrete increased gradually in the compression zone, whereas, there was barely any confinement in the tensile zone. The CFRTs under bending generally showed good ductility. The typical failure modes of all specimens were the overall bending, and the failure shapes were close to a half-sine wave.

(2) FE models for the CFRTs were developed and verified against the test results. Parametric study was also performed to extensively investigate the influence of different parameters on the behavior of the CFRTs using the validated FE modeling approach. It was found that with the increase of concrete strength and steel strength, the ultimate moment of the CFRTs increased, while the flexural stiffness remained almost unchanged. Moreover, the aspect ratio has much more significant influence on the flexural performance of the specimens bending about the major axis than those bending about the minor axis.

(3) Practical formulas for the flexural stiffness and ultimate moment of the CFRTs were established, and a simplified model of the moment vs. curvature curve was also proposed. Reasonable agreement was achieved in the comparison of the ultimate moment and flexural stiffness between experimental, FE and predicted results by the proposed formula. Moreover, the proposed formula in this paper was capable for predicting the ultimate moment of CFRTs under bending. The proposed formulas in this paper are based on the results of both test and numerical parametric study. Therefore, it is supposed that they can be applied for concrete grades range from C40 to C100, steel strengths range from 235 to 420 MPa, and the steel ratio from 0.02 to 0.08, which are also commonly used in engineering practice.

Acknowledgments

This research work is financially supported by the National Natural Science Foundation of China, Grant No. 51578548, and the National Key Research Program of China, Grant No. 2017YFC0703404.

References

AIJ (1997), *Recommendations for Design and Construction of Concrete Filled Steel Tubular Structures*, Architectural Institute of Japan, Tokoy.

AISC (1999), *Load and Resistance Factor Design Specification for Structural Steel Buildings (IL)*, American Institute of Steel Construction, Chicago.

Aslani, F., Uy, B. and Tao, Z. (2015), "Predicting the axial load capacity of high-strength concrete filled steel tubular columns", *Steel Compos. Struct*., **19**(4), 967-993.

BS5400 (2005), *Part 5. Concrete and Composite Bridges*, British Standards Institutions, London.

CECS28 (2012), *Technical Specification for Concrete-Filled Steel Tubular Structures*, China Planning Press, Beijing, China.

Chang, X., Luo, X.L., Zhu, C.X. and Tang, C.N. (2014), "Analysis of circular concrete-filled steel tube support in high ground stress conditions", *Tunn. Undergr. Sp Tech*., **43**(6), 41-48.

Chang, X., Ru, Z.L., Zhou, W. and Zhang, Y.B. (2013), "Study on concrete-filled stainless steel carbon steel tubular (CFSCT) stub columns under compression", *Thin Wall. Struct*., **63**(2), 125-133.

Chen, B.L. and Wang, L.G. (2015), "Experimental study on flexural behavior of splicing concrete-filled gfrp tubular composite members connected with steel bars", *Steel Compos. Struct*., **18**(5), 1129-1144.

Chen, J., Wang, J. and Xie, F. (2016), "Behavior of thin-walled dodecagonal section double skin concrete-filled steel tubes under bending", *Thin Wall. Struct*., **98**(1), 293-300.

Chitawadagi, M.V. and Narasimhan, M.C. (2009), "Strength deformation behaviour of circular concrete filled steel tubes subjected to pure bending", *J. Constr. Steel Res*., **65**(5), 1567-1591.

DBJ13-51-2003 (2003), *Technical Code for Concrete Filled Steel Tubular Structures*, Housing and Urban-Rural Development of Fujian, Fuzhou, China.

Ding, F.X., Fu, L. and Liu, X.M. (2016), "Mechanical performances of track-shaped rebar stiffened concrete-filled steel tubular (SCFRT) stub columns under axial compression", *Thin Wall. Struct*., **99**(2), 168-181.

Ding, F.X., Fu, L. and Yu, Z.W. (2015), "Mechanical performance of concrete-filled steel tubular stub columns with round ends under axial loading", *Thin Wall. Struct*., **97**(12), 22-34.

DL/T5085-1999 (1999), *Code for Design of Steel-Concrete Composite Structure*, China Electric Power Press, Beijing, China.

Eurocode 4 (2004), *Design of Steel and Concrete Structures. Part1. 1: General Rules and Rules for Building*, European Committee for Standardization, Brussels (Belgium).

GB/T228-2002, China Standard (2002), *Metallic materials-tensile testing at ambient temperatures*, Standards Press of China, Beijing, China.

GB/T50081-2002, China Standard (2002), *Standard for method of mechanical properties on ordinary concrete*, China Building Industry Press, Beijing, China.

GB50936-2014 (2014), *Technical Code for Concrete Filled Steel Tubular Structures*, China Building Industry Press, Beijing, China.

Han, L.H., Lu, H. and Yao, G.H. (2006), "Further study on the flexural behavior of concrete-filled steel tubes", *J. Constr. Steel Res*., **62**(6), 554-565.

Hassanein, M.F. and Kharoob, O.F. (2014), "Analysis of circular concrete-filled double skin tubular slender columns with external stainless steel tube", *Thin Wall. Struct*., **79**(6), 23-37.

Hassanein, M.F., Kharoob, O.F. and Liang, Q.Q. (2013), "Circular concrete-filled double skin tubular short columns with external stainless steel tubes under axial compression", *Thin Wall. Struct*., **73**(12), 252-263.

Hibbitt, Karlson & Sorensen Inc. (2003), ABAQUS/standard User's Manual, Version 6.4.1.,Pawtucket, RI, USA.

Kim, J.K., Kwak, H.G. and Kwak, J.H. (2013), "Behavior of hybrid double skin concrete filled circular steel tube columns", *Steel Compos. Struct*., **14**(14), 191-204.

Liu, J., Ding, F.X., Liu, X.M. and Yu, Z.W. (2016), "Study on flexural capacity of simply supported steel-concrete composite beam", *Steel Compos. Struct*., **21**(4), 829-847.

Moon, J., Roeder, C.W. and Lehman, D.E. (2012), "Analytical modeling of bending of circular concrete filled steel tubes", *Eng. Struct*., **42**(7), 58-66.

Uenaka, K. and Tsunokake, H. (2016), "Concrete filled elliptical steel tubular members with large diameter-to-thickness ratio subjected to bending", *Structures*., **5**(2), 58-66.

Uenaka, K., Kitoh, H. and Sonoda, K. (2008), "Concrete filled double skin tubular members subjected to bending", *Steel Compos. Struct*., **8**(4), 297-312.

Wan, C.Y. and Zha, X.X. (2016), "Nonlinear analysis and design of concrete-filled dual steel tubular columns under axial loading", *Steel Compos. Struct*., **20**(3), 571-597.

Wang, Q.T. and Chang, X. (2013), "Analysis of concrete-filled steel tubular columns with "T" shaped cross section (CFTTS)", *Steel Compos. Struct*., **15**(1), 41-45.

Wang, R., Han, L.H. and Nie, J.G. (2014), "Flexural performance of rectangular CFST members", *Thin Wall. Struct*., **79**(6), 154-165.

Xie, J.X., Tang, P.Z. and Lu, A. (2011), "Modal analysis and experimental study on round-ended CFST coupled column cable stayed bridge, Mechanic Automation and Control Engineering (MACE)", *Proceedings of the 2nd International Conference on. IEEE.*

BU